

Supplementary Information:

Current Induced Phase Segregation in Mixed Halide
Hybrid Perovskites and its Impact on Two-Terminal
Tandem Solar Cell Design

*Ian L. Braly^{1†}, Ryan J. Stoddard^{1†}, Adharsh Rajagopal², Alexander R. Uhl¹, John K. Katahara¹,
Alex K.-Y. Jen^{2,3} and Hugh W. Hillhouse^{1*}*

¹Department of Chemical Engineering, Clean Energy Institute, and Molecular Engineering & Sciences Institute, University of Washington, Seattle, Washington 98195-1652, United States

²Department of Materials Science and Engineering, University of Washington, Seattle, WA 98195-2120, United States.

³Department of Materials Science & Engineering, City University of Hong Kong, Kowloon, Hong Kong

[†]Equal author contribution

*Corresponding author. Email: h2@uw.edu; Ph 1-206-685-5257 (H.W.H).

Methods:

Film Preparation

(FA_{0.83},Cs_{0.17})Pb(I_{0.66},Br_{0.34})₃: All films were prepared on pre-cleaned glass substrates which were further cleaned with four 10-minute sonication steps with 5% Alconox in deionized (DI) water, pure DI water, acetone, and 2-propanol, followed with plasma cleaning in Ar plasma for 10 minutes. (FA_{0.83},Cs_{0.17})Pb(I_{0.66},Br_{0.34})₃ precursor solutions were prepared from FAI, CsI, PbI₂ and PbBr₂ with a 1.0M solution in 8/2 vol/vol dimethylformamide (DMF)/DMSO solution. Solution was heated to 70 °C then stirred for 90 min then filtered after cooling down with a 0.2 μm PTFE filter. These films were spin coated with a 2-step program: 8 s at 1000 rpm then 20 s at 4000 rpm. 0.7mL toluene was dispensed on the spinning substrate with 15 s remaining in the final step. We note that DMF films require precise dispensing of toluene to get smooth, crack-free films, and the length of the first step in the spin coating program may need to be adjusted based on a different spin coater. (FA_{0.83},Cs_{0.17})Pb(I_{0.66},Br_{0.34})₃ “high-temperature” (FACs-HT) films were annealed at 165 °C for 50 min and (FA_{0.83},Cs_{0.17})Pb(I_{0.66},Br_{0.34})₃ “low-temperature” (FACs-LT) films were annealed at 75 °C for 10 min. The thickness of the FACs-HT and FACs-LT films were measured by profilometry to be 320 nm and 320 nm, respectively. All ink mixing, spin coating, and annealing steps were performed in a N₂-filled glovebox.

MAPb(I_{0.6}Br_{0.4})₃ and (MA_{0.9},Cs_{0.1})Pb(I_{0.6}Br_{0.4})₃: Sequential steps of ultrasonication for 10 min in detergent, deionized water, acetone, and isopropanol alcohol were used to clean glass substrates. MAPb(I_{0.66}Br_{0.34})₃ and (MA_{0.9},Cs_{0.1})Pb(I_{0.6}Br_{0.4})₃ precursor solutions were prepared from MAI, CsI, PbI₂, and PbBr₂ in mixed solvent (volume ratio 3:7) of DMSO and γ-butyrolactone (GBL); solutions were stirred at 60 °C for 1 h. Cleaned substrates were transferred into N₂-filled glovebox for film deposition. The perovskite precursor solution was spin coated onto the substrate using 2-step spin program (1000 rpm for 15 s and 4000 rpm for 45 s); during the last 20-10 s of the second spin-coating step, 0.7 ml toluene was dropped onto the spinning substrate and the substrates were annealed at 100°C for 10 min. The thickness of the MA and MACs films were measured by profilometry to be 202 nm and 194 nm, respectively.

Device Fabrication

(FA_{0.83},Cs_{0.17})Pb(I_{0.66},Br_{0.34})₃: ITO glass (15 ohm/sq, Colorado Concept Coatings) was cleaned with sonication and Ar plasma as described above. Cu:NiOx solution was prepared for the conventional sol-gel method as described elsewhere¹ with 5 mol% Cu to Ni. Cu:NiOx layer was fabricated by spin coating at 3000 rpm for 60 s then annealing at 350 °C for 60 min in air. Next, films were transferred into a N₂-filled glovebox for perovskite layer deposition as described above. PCBM (15mg/mL in chlorobenzene) was spin coated at 1000 rpm for 60 s then bis-C₆₀ (2mg/mL in 2-propanol) was spin coated at 3000 rpm for 30 s. Finally, 150nm Ag was thermally evaporated at a rate of 2 Å/s with shadow masks (3.14 mm²).

MAPb(I_{0.6}Br_{0.4})₃ and (MA_{0.9}Cs_{0.1})Pb(I_{0.6}Br_{0.4})₃: ITO glass was cleaned with sonication and UV ozone treatment as described above. A NiO_x precursor solution was prepared by dissolving 124.4 mg of Nickel (II) acetate tetrahydrate in 5 mL ethanol and 30 μL ethanolamine was added to it; the mixture was stirred at 60 °C for 2 h. The NiO_x precursor was spin coated onto the clean ITO glass at 3000 rpm for 60 s and annealed at 400°C for 1 h in ambient. Next, films were transferred into a N₂-filled glovebox for perovskite layer deposition as described above for MA containing films. For the ETL precursor solution, 15 mg/mL PC₆₁BM was dissolved in chloroform and stirred at 80 °C for 30 min. The PC₆₁BM solution was spin coated using 4000 rpm for 45 s followed by annealing at 100 °C for 5 min. For the fullerene surfactant solution, 2 mg/mL Bis-C60 in isopropyl alcohol was dissolved using sonication (typically 1 h). The bis-C₆₀ surfactant solution was spin coated on top at 3000 rpm for 60 s. Finally, 150 nm thick silver (Ag) electrode was evaporated under high vacuum ($<1 \times 10^{-6}$ Torr) with shadow masks (3.14 mm²). All solutions were filtered with 0.22 μm PVDF filters before spin coating. Figure S5 refers to “MA-thin” and “MA-thick” devices. The “MA-thin” devices were fabricated using the method described here and had an absorber layer thickness of 202 nm, while the “MA-thick” devices were fabricated using the methods described above in the paragraph labeled “(FA_{0.83}Cs_{0.17})Pb(I_{0.66}Br_{0.34})₃” using the same ink concentration but different solute composition. The absorber layer thickness for the “MA-thick” devices were measured by profilometry to be 360 nm.

Non-injecting lateral devices for electric field experiment

Lateral devices with back contact architecture were used to separate the effect of electric field and charge injection on phase segregation. Each device consisted of two Au electrodes separated by a 10 μm channel (Figure S6). A dielectric layer was deposited on top of the electrodes to prevent direct charge injection into the perovskite material deposited within the channel. Devices were fabricated at the Washington Nanotechnology Facility (WNF) using photolithography and liftoff. 100 mm Si wafers with a 1 μm layer of thermal oxide were coated with a thin layer of NR9 negative photoresist (3000py) through spincoating followed by a post-bake at 150 °C for one minute. The photoresist was exposed for 40s under UV excitation in an ABM contact aligner, followed by a 40 s post bake at 110 °C. After the resist was developed, the wafers were coated with 10 nm Ti (adhesion layer) and 150 nm Au through e-beam evaporation. After liftoff in an acetone bath, the wafers were coated with 50 nm of Al₂O₃ through thermal atomic layer deposition at 300 °C.

CIGS device fabrication:

The CIGS device used in this work was fabricated using the methods described in Ref. 38 of the main text.²

SEM and XRD

SEM micrographs were collected using an FEI XL830 Dualbeam SEM-FIB on Au-sputtered perovskite films. Film thickness was determined using a Bruker-DektakXT profilometer.

X-ray diffraction spectra shown in Figure 1d were collected using a Bruker D8 Discover with GADDS (General Area Detector Diffraction System), a Cu anode ($\lambda = 1.542 \text{ \AA}$) and Hi-Star 2D detector. The instrument was operated in parallel-beam geometry with a 0.5 mm beam diameter. The instrument related peak broadening was determined to be 0.3° in 2θ based on a NIST corundum standard. The (200) diffraction peaks shown in Figure 1e were collected using a Bruker D8 Advance with a Lynxeye detector. The instrument was operated in Bragg-Brentano geometry. The instrument related peak broadening was determined to be 0.04° in 2θ based on a NIST corundum standard.

Photoluminescence and Electroluminescence Experiments:

Absolute intensity confocal PL was conducted in similar procedure as described previously.^{3,4} PL spectra were obtained with a modified Horiba LabRAM HR-800 with 532nm laser excitation and 10x objective. The adjustable confocal hole was set to 800 μm and a 150 gr/mm Czerny-Turner monochromator blazed at 500 nm was used. The photon detection rate was calibrated using a blackbody source (IR-301, Infrared Systems Development) at 850, 950 and 1050 $^\circ\text{C}$ with 10 μm pinhole (calibration factor was averaged between three temperatures to minimize error). To calculate 1 sun excitation flux, an Oriel optical power meter and beam profiler was used to set photon flux equal to above-bandgap photon flux of AM1.5 GT solar spectrum for a 1.75 eV material. All confocal PL measurements were conducted in a closed, N_2 -filled stage (Linkam Scientific LTSE420-P) with continuous N_2 purge at 70% of maximum flow, with the stage temperature regulated to 20 $^\circ\text{C}$.

Electroluminescence data was collected with the same set up as confocal PL (Horiba Labram with 150 gr/mm grating blazed at 500nm), but using current injection with Keithley 2400 rather than 532nm photoexcitation. EL experiments were also conducted in N_2 -filled Linkam stage with constant N_2 purge and temperature regulated to 20 $^\circ\text{C}$.

J-V measurements were conducted in air using a Keithley 2400 SourceMeter Newport Oriel Sol3a Class AAA Solar Simulator calibrated to 1 Sun AM1.5 GT using Newport 91150V Si reference diode. J-V curves were collected with a reverse voltage sweep at a slow sweep rate of 75 mV/s. Device area was 3.14 mm^2 defined by Ag contact area (valid due to high resistance in all HP/ETL/HTL layers). Maximum power point data were collected in a N_2 -filled glovebox with 450 W Oriel xenon lamp calibrated to AM1.5 GT.

Supplemental Figures:

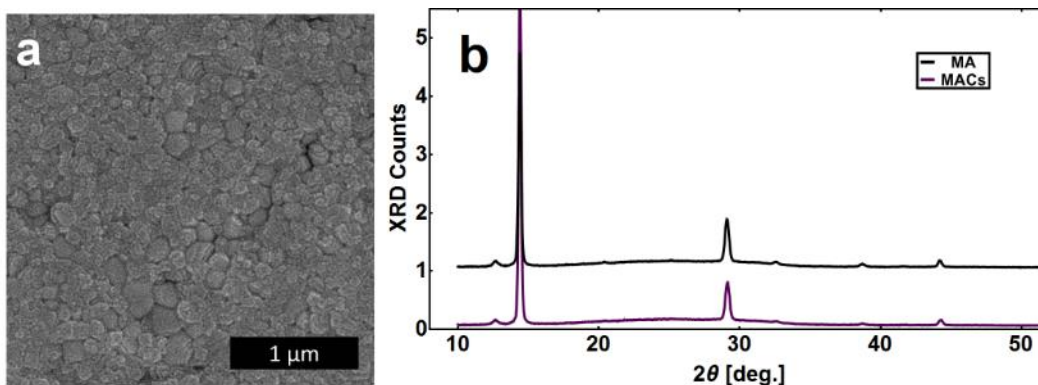


Figure S1. (a) Top-view SEM micrograph of a $(\text{MA}_{0.9},\text{Cs}_{0.1})\text{Pb}(\text{I}_{0.4},\text{Br}_{0.6})_3$ thin film annealed at 100°C for 10 minutes. (b) XRD patterns of the same film (labeled MACs -- $\text{MAPb}(\text{I}_{0.4},\text{Br}_{0.6})_3$) XRD pattern from the main text shown for reference).

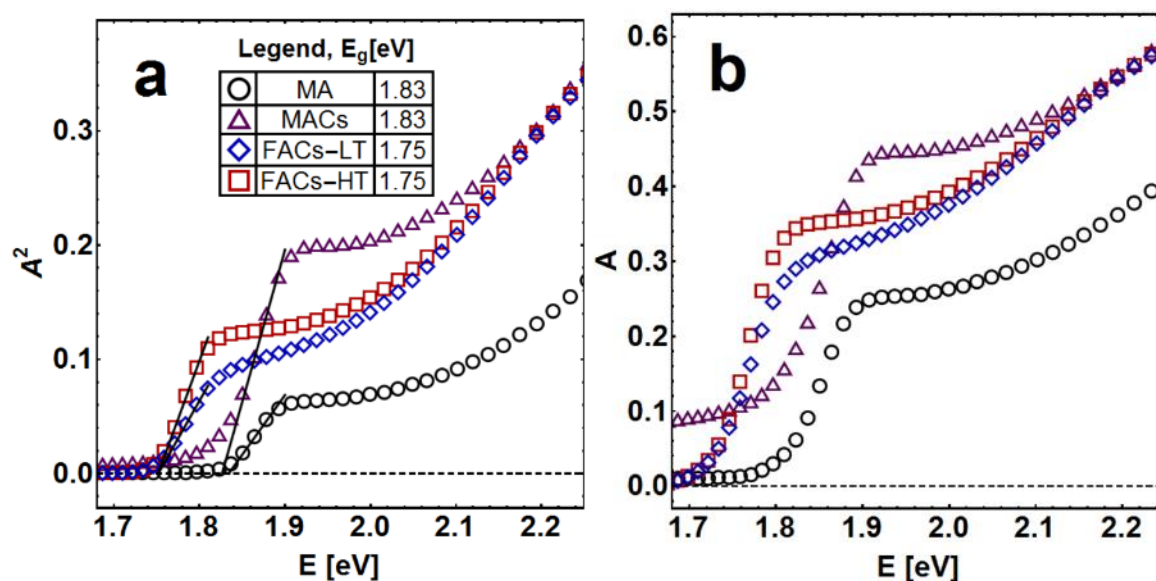


Figure S2: vis-NIR spectra for bandgap extraction of the samples of $\text{MAPb}(\text{I}_{0.6},\text{Br}_{0.4})_3$ (black circles), $(\text{MA}_{0.9},\text{Cs}_{0.1})\text{Pb}(\text{I}_{0.6},\text{Br}_{0.4})_3$ (purple triangles), $(\text{FA}_{0.83},\text{Cs}_{0.17})\text{Pb}(\text{I}_{0.66},\text{Br}_{0.34})_3$ annealed at 75°C (blue diamonds), and the $(\text{FA}_{0.83},\text{Cs}_{0.17})\text{Pb}(\text{I}_{0.66},\text{Br}_{0.34})_3$ annealed at 165°C (red squares). a) Absorbance-squared plotted against photon energy, and b) absorbance plotted against photon energy.

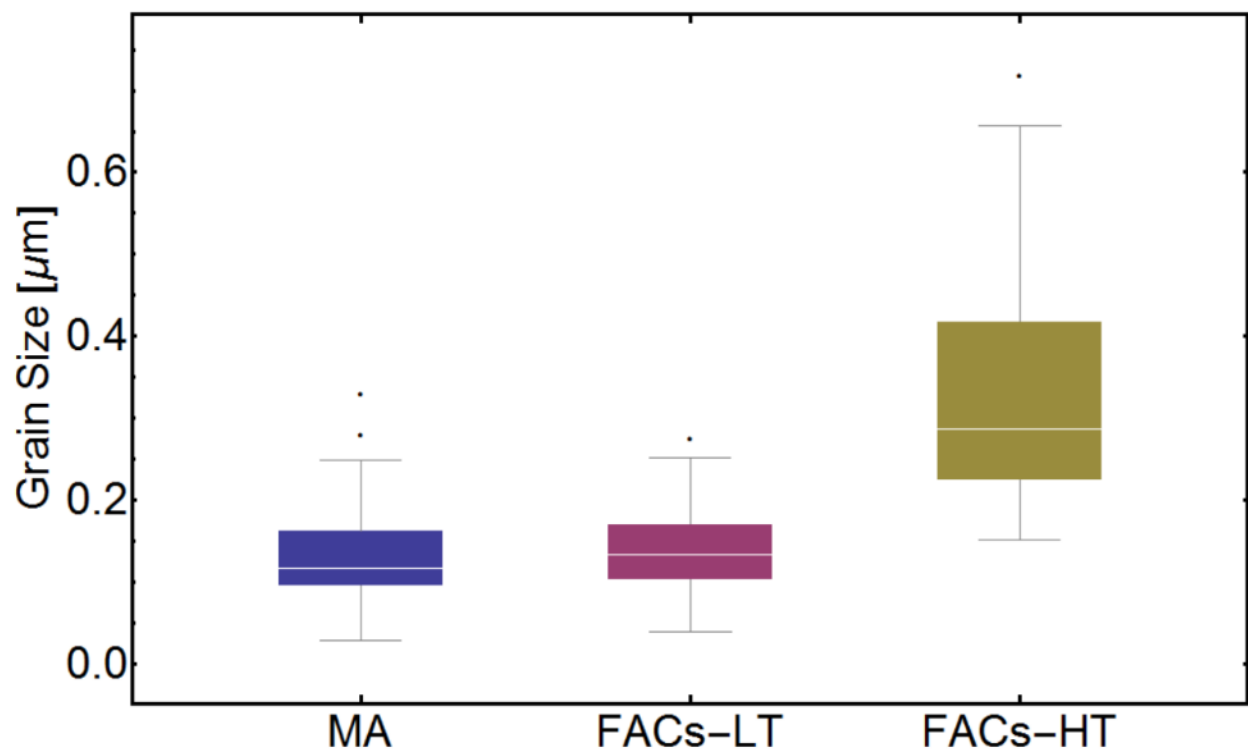


Figure S3: Morphological grain size (determined from top-down SEM images) box-and-whisker plot of the $\text{MAPb}(\text{I}_{0.6}, \text{Br}_{0.4})_3$, $(\text{FA}_{0.83}, \text{Cs}_{0.17})\text{Pb}(\text{I}_{0.66}, \text{Br}_{0.34})_3$ annealed at 75°C , and the $(\text{FA}_{0.83}, \text{Cs}_{0.17})\text{Pb}(\text{I}_{0.66}, \text{Br}_{0.34})_3$ annealed at 165°C .

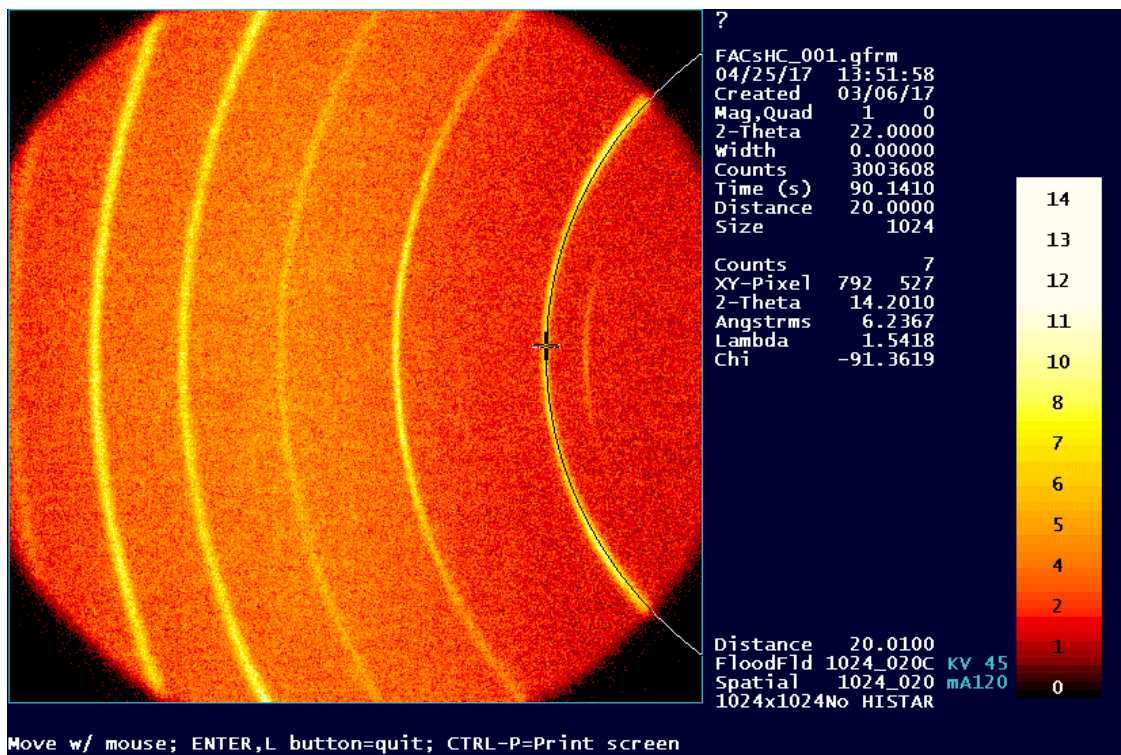


Figure S4: Two dimensional XRD detector image of a $(\text{FA}_{0.84}\text{Cs}_{0.16})\text{Pb}(\text{I}_{0.6}\text{Br}_{0.4})_3$ thin film annealed at 165°C .

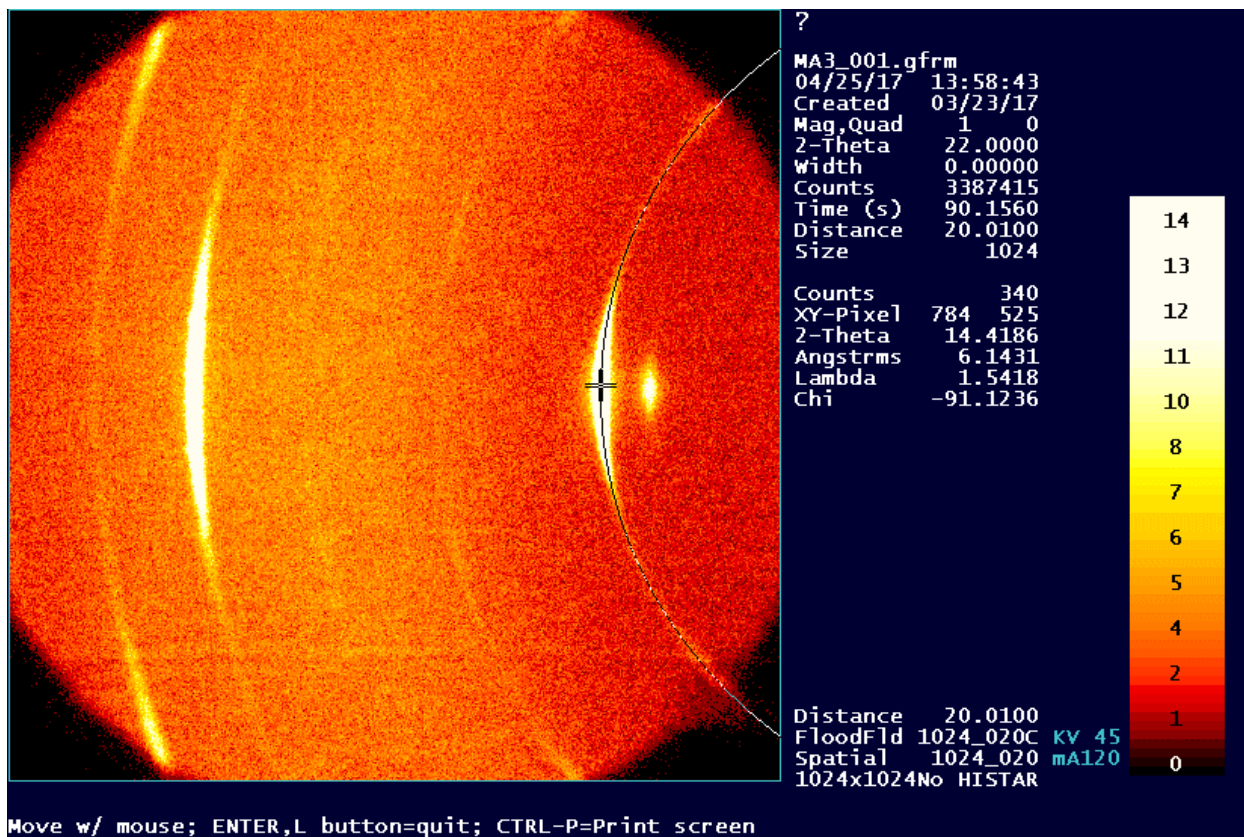


Figure S5: Two dimensional XRD detector image of a $\text{MAPb}(\text{I}_{0.6}\text{Br}_{0.4})_3$ thin film annealed at 110°C .

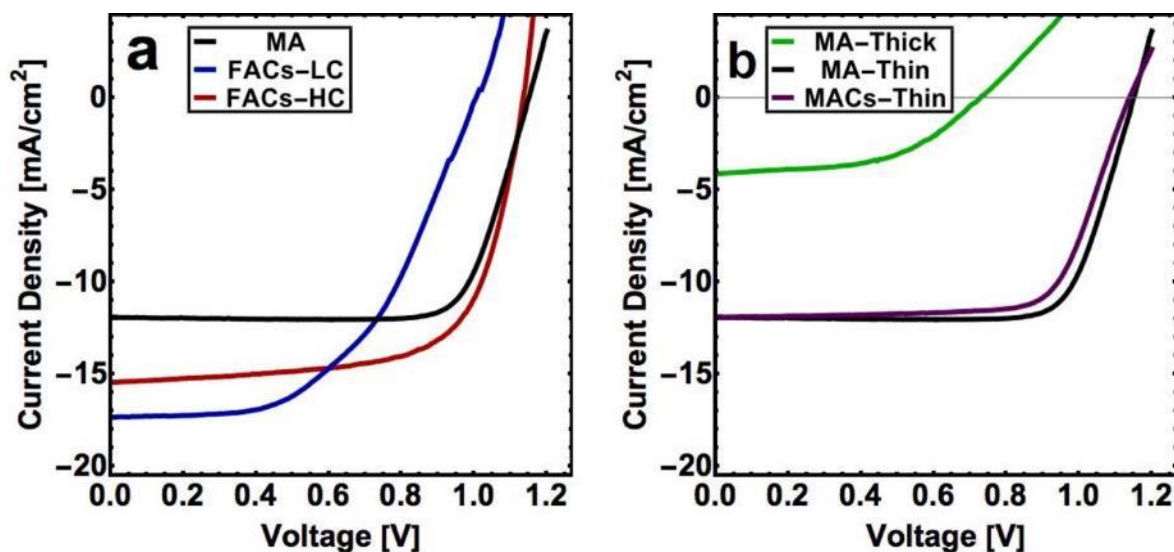


Figure S6 (a) Current-voltage (JV) sweeps of devices utilizing a 202 nm $\text{MAPb}(\text{I}_{0.6}, \text{Br}_{0.4})_3$ absorber (black), low temperature annealed, 330 nm $(\text{FA}_{0.83}, \text{Cs}_{0.17})\text{Pb}(\text{I}_{0.34}, \text{Br}_{0.66})_3$ absorber (blue), and high temperature annealed, 320 nm $(\text{FA}_{0.83}, \text{Cs}_{0.17})\text{Pb}(\text{I}_{0.34}, \text{Br}_{0.66})_3$ absorber (red). (b) JV curves for MACs-Thin (194 nm thick absorber) and MA-Thick (364 nm absorber) devices. MACs-Thin device performance is very similar to MA-thin (same as MA in part a).

MA-thick devices have comparable thickness to FACs devices discussed in text, yet they have very low J_{SC} and power conversion efficiency. Therefore, we used devices with thinner perovskite absorber layers for the EL experiments (MA-Thin and MACs-Thin) in the characterization and analysis discussed in main text. (MA-thin curve in (b) is the same as MA curve in (a)). The reasonable performance of the thinner MA-containing devices makes them more relevant for the EL and PL experiments in this work, however the authors note that film thickness can play a significant role in light absorbance and diffusion of the species.⁵

Table S1: JV Device Parameters

	MA	MACs	FACs-LT	FACs-HT
PCE [%]	10.6	9.7	9.01	11.9
V_{OC} [V]	1.15	1.14	1.01	1.13
J_{SC} [mA/cm^2]	11.8	11.9	17.3	15.4
FF [%]	78.1	71.9	51.5	67.7

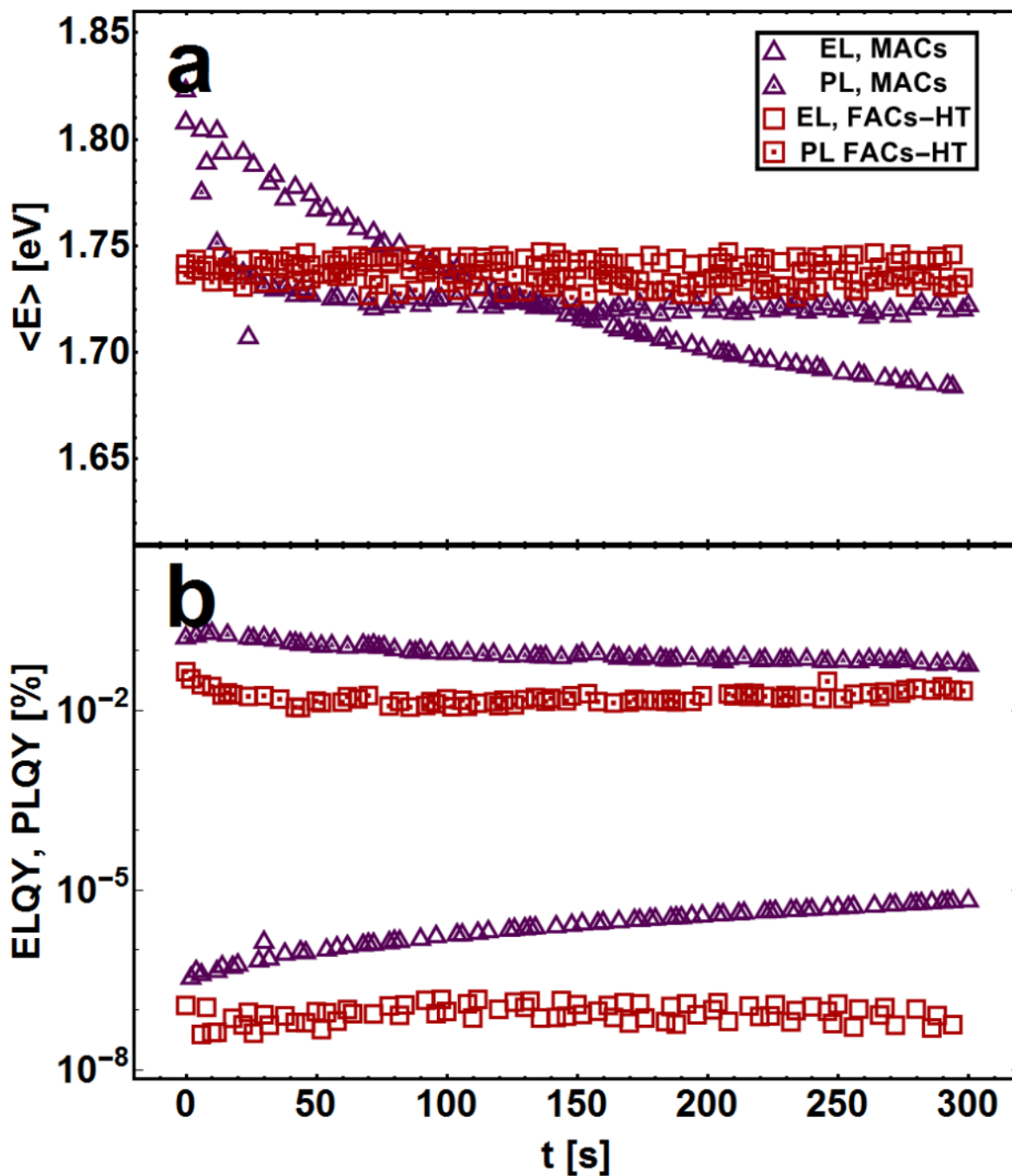


Figure S7: Electroluminescence and photoluminescence measurements over time. (a) Mean electroluminescence and photoluminescence emission energy of devices utilizing $(\text{MA}_{0.9}, \text{Cs}_{0.1})\text{Pb}(\text{I}_{0.6}\text{Br}_{0.4})_3$ and high temperature annealed $(\text{FA}_{0.83}, \text{Cs}_{0.17})\text{Pb}(\text{I}_{0.34}\text{Br}_{0.66})_3$ absorbers. (b) external electroluminescence and photoluminescence quantum yield from the same experiment.

In the main text, we claimed that, in addition to carrier funneling, the forcing function that governs photon emission will make the intensity of the low energy peak stronger relative to the high energy peak during luminescence of a phase segregating hybrid perovskite film. Consider two cases, where in the initial case a large-bandgap material with a steep subbandgap tail is emitting photons commensurate with a quasi Fermi-level splitting of $\Delta\mu_1$; and in the final case the material has developed a broader subbandgap tail extends to lower energies similar to what is observed in a phase segregating large-bandgap hybrid perovskite, but is still emitting photons commensurate with a quasi Fermi-level splitting of $\Delta\mu_2 = \Delta\mu_1$. We are interested in the relative emission intensity at two energies, E_1 and E_2 , which have the same absorption coefficients, $\alpha_1(E_1)$ and $\alpha_2(E_2)$. Since the subbandgap tail is broader and red shifted, E_1 is larger than E_2 . Summarizing the two cases,

$$\alpha_1(E_1) = \alpha_2(E_2) \quad (S1)$$

$$\Delta\mu_1 = \Delta\mu_2 \quad (S2)$$

$$E_1 > E_2 \quad (S3)$$

The emission in each case will be determined by the Generalized Planck Law, shown in Equation S1,

$$I_{PL}(E) = \left\{ \frac{2\pi E^2}{h^3 c^2} \right\} \left\{ \frac{1}{\text{Exp}\left(\frac{E-\Delta\mu}{kT}\right)-1} \right\} a(E) \quad (S4)$$

where the expression in the first curly brackets is the photon density of states, the expression in the second curly brackets is the Bose-Einstein distribution, and the final term is the absorptivity. Taking the ratio of the final emission intensity at E_f to the initial emission intensity at E_i , taking the Wein approximation, and cancelling equal terms,

$$I_{PL,2}/I_{PL,1} = \frac{E_2}{E_1} \text{Exp}\left[\frac{E_2-E_1}{kT}\right] \quad (S5)$$

Figure S6 shows Equation S5 plotted assuming E_1 is 1.75 eV and T is 298 K.

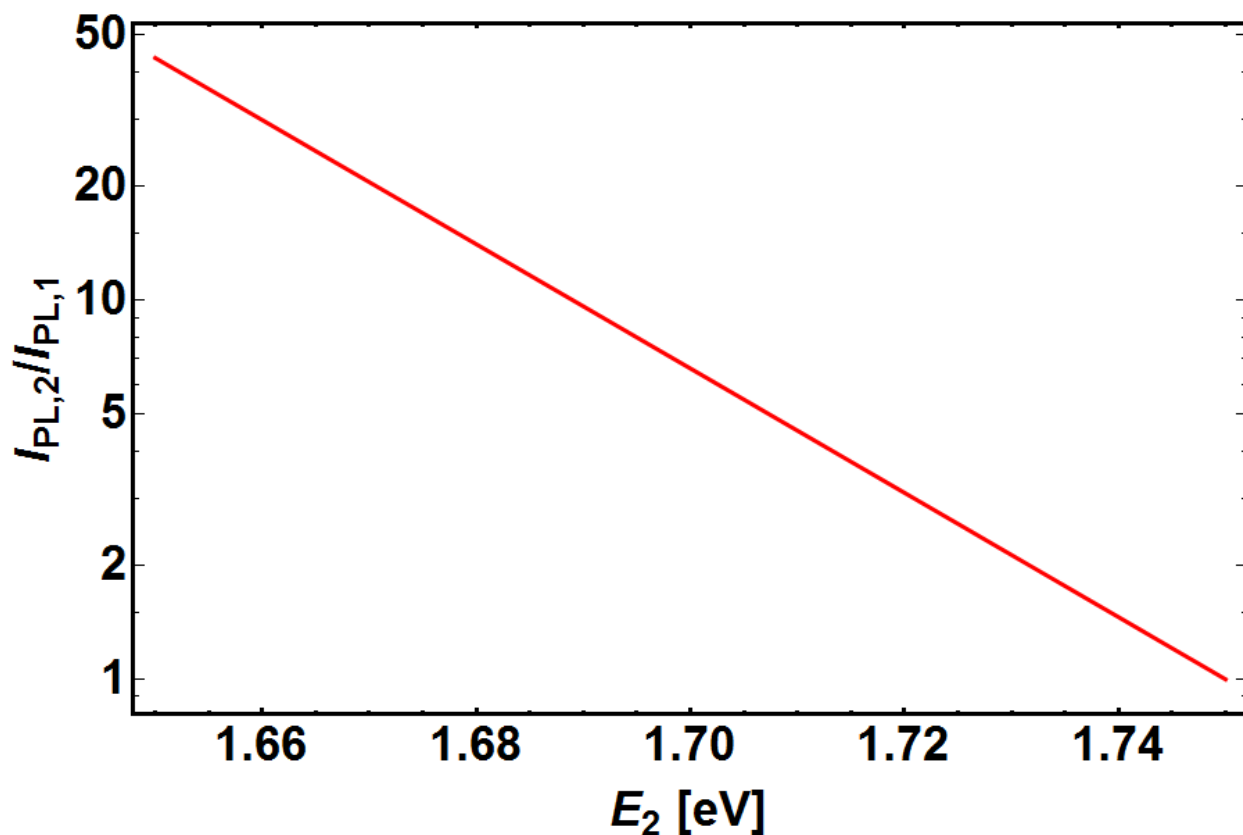


Figure S8: Final luminescence intensity at E_2 relative to that at E_1 as a function of final luminescence energy E_2 for a red-shifting band edge, assuming no change in quasi-Fermi level splitting and assuming no change in the density of states (only a shift of the density of states to a lower energy).

The luminescence intensity at lower energy grows exponentially as the band edge red shifts from 1.75 to 1.65 eV, increasing by a factor of 50 assuming no changes in the quasi Fermi level splitting and that the density of states does not change in magnitude but only shifts to lower energy. In reality, the increase should not be this high since not all of the film phase segregates and the density of states at the lower energy is likely lower. But without measurement of the density of states of the phase segregated domains and the extent of phase segregation, the increase in PLQY cannot be precisely allocated to either the carrier funneling mechanism or the expected increased driving for emission.

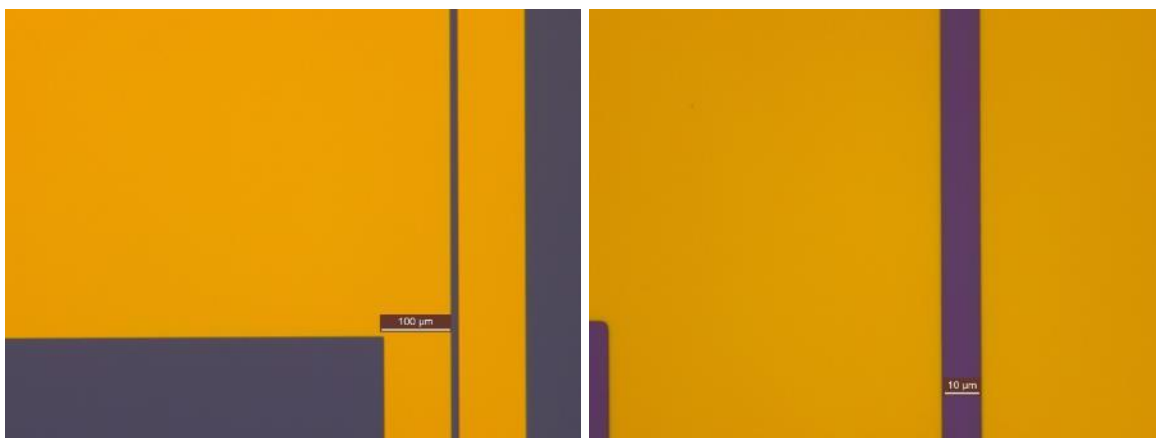


Figure S9: Microscope images of the insulated interdigitated back contact substrates used to determine the impact of electric field only on phase segregation of an MA film. (Left) A 10x magnification image of one of the gold contact pads shown in the top left portion of the image and a 10 micron channel spanning from the top to bottom of the image. (Right) a 50x magnification image of the 10 micron channel.

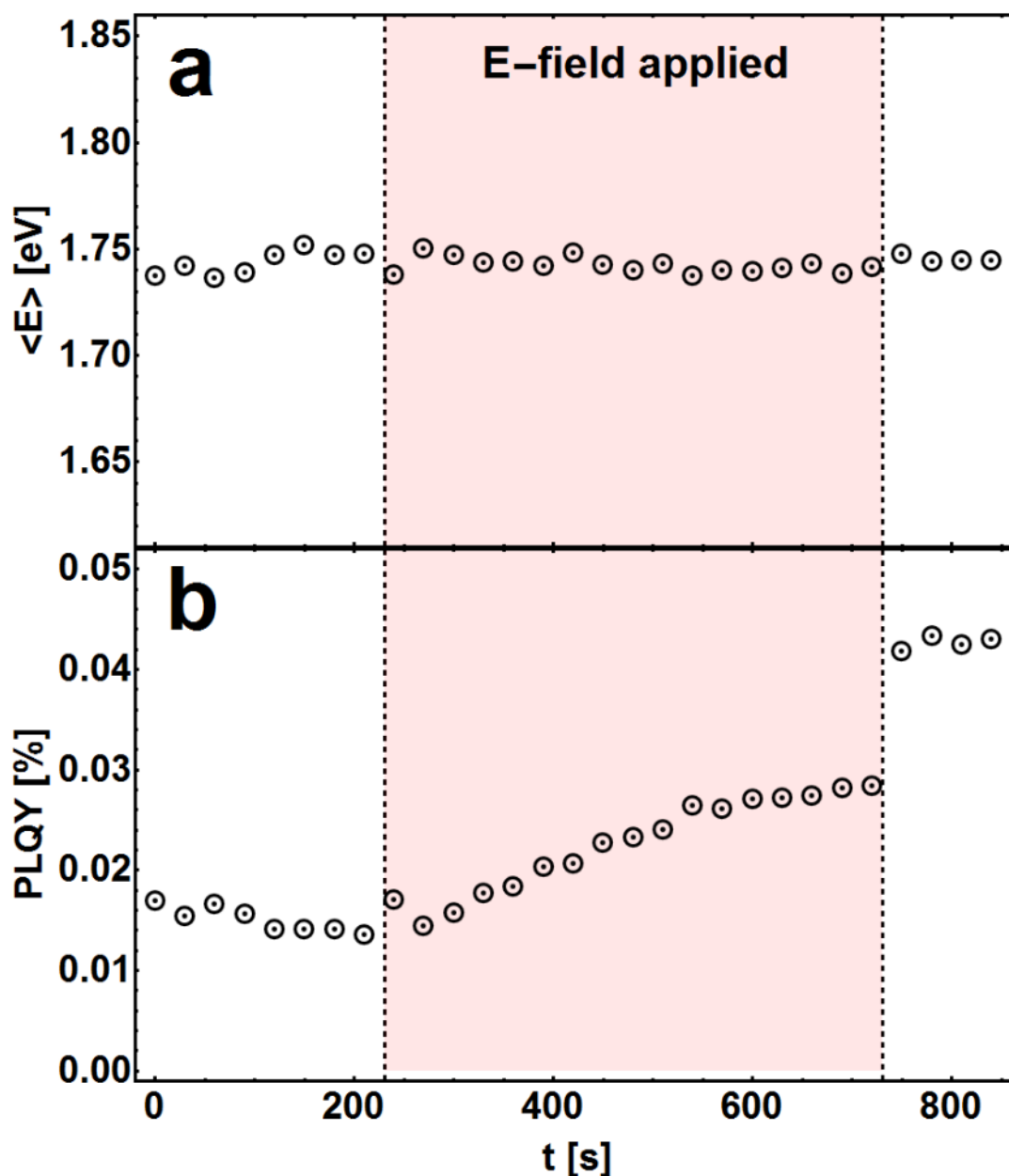


Figure S10: PL of an MA film deposited on insulated interdigitated back-contacts. A 532 nm CW-laser was turned on for less than a second for each collection, keeping the film in the dark for the remainder of the experiment. After 230 s, 60 V were applied across the 10-micron channel, and at 730 s the applied voltage was switched off, as depicted by the light red region in the plot. (a) Mean photoluminescence emission energy over time. Phase segregation is not observed, indicating that an applied electric field (in the absence of charge injection) does not cause phase segregation. (b) Photoluminescence quantum yield over time. Gradual PLQY increase is observed during electric field application followed by a jump in PLQY is observed upon field cessation. This is likely related to the build-up and relaxation of energy storage from ionic charge separation induced by the electric field application, however the authors can only speculate without a further detailed study.

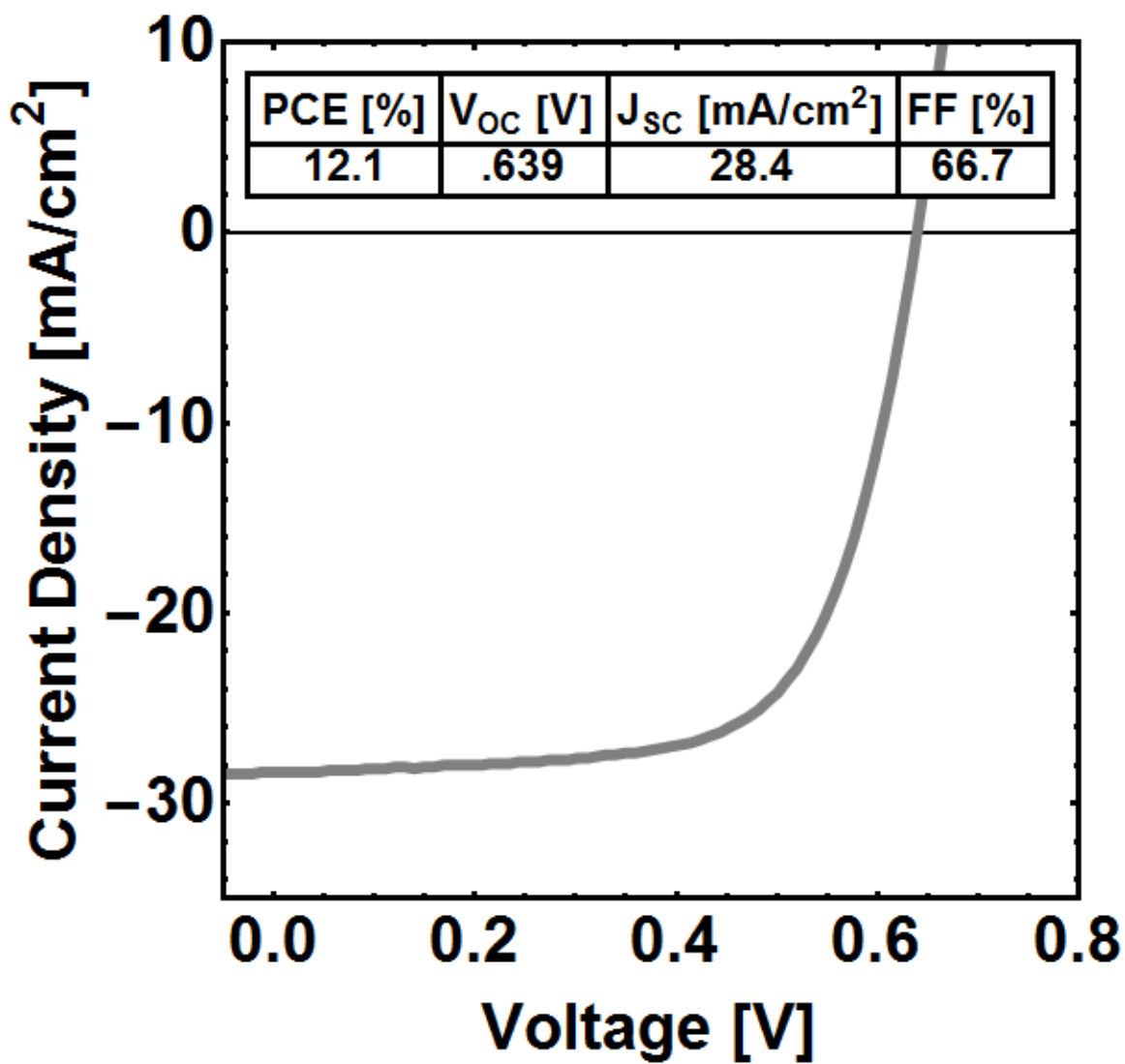


Figure S11: Current density-voltage relationship for the Cu(In,Ga)Se₂ cell used to collect the data in Figure 4 c of the main text. The inset table reports the power conversion efficiency, open-circuit voltage, short-circuit current density, and fill-factor of this device.

References

- (1) Jung, J. W.; Chueh, C.-C.; Jen, A. K. Y. A Low-Temperature, Solution-Processable, Cu-Doped Nickel Oxide Hole-Transporting Layer via the Combustion Method for High-Performance Thin-Film Perovskite Solar Cells. *Adv. Mater.* **2015**, *27* (47), 7874-7880.
- (2) Uhl, A., R.; Yang, Z.; Jen, A. K.-Y.; Hillhouse, H. W. Solution-Processed Chalcopyrite-Perovskite Tandem Solar Cells in Bandgap-Matched Two- and Four-Terminal Architectures. *J. Mat. Chem. A* **2017**, *5*, 3214-3220.
- (3) Katahara, J. K.; Hillhouse, H. W. Quasi-Fermi Level Splitting and Sub-Bandgap Absorptivity from Semiconductor Photoluminescence. *J. Appl. Phys.* **2014**, *116*, 173504.
- (4) Braly, I. L.; Hillhouse, H. W. Optoelectronic Quality and Stability of Hybrid Perovskites from MAPbI₃ to MAPbI₂Br Using Composition Spread Libraries. *J. Phys. Chem. C* **2016**, *120*, 893-902.
- (5) Hoffman, J. B.; Schleper, A. L.; Kamat, P. V. Transformation of Sintered CsPbBr₃ Nanocrystals to Cubic CsPbI₃ and Gradient CsPbBr_xI_{3-x} through Halide Exchange. *J. Am. Chem. Soc.* **2016**, *138*, 8603-8611.